Published in final edited form as:

IEEE Trans Med Imaging. 2020 November ; 39(11): 3559–3570. doi:10.1109/TMI.2020.2999439.

Shear Induced Non-linear Elasticity Imaging: Elastography for Compound Deformations

Soumya Goswami [Student Member, IEEE], **Rifat Ahmed [Student Member, IEEE]**, **Siladitya Khan [Student Member, IEEE]**, **Marvin M. Doyley [Member, IEEE]**, **Stephen A. McAleavey [Member, IEEE]**

Hajim School of Engg. and Applied Sciences, University of Rochester, Rochester, NY 14627 USA

Abstract

The goal of non-linear ultrasound elastography is to characterize tissue mechanical properties under finite deformations. Existing methods produce high contrast non-linear elastograms under conditions of pure uni-axial compression, but exhibit bias errors of 10–50 % when the applied deformation deviates from the uni-axial condition. Since freehand transducer motion generally does not produce pure uniaxial compression, a motion-agnostic non-linearity estimator is desirable for clinical translation. Here we derive an expression for measurement of the Non-Linear Shear Modulus (NLSM) of tissue subject to combined shear and axial deformations. This method gives consistent nonlinear elasticity estimates irrespective of the type of applied deformation, with a reduced bias in NLSM values to 6–13 %. The method combines quasi-static strain imaging with Single-Track Location-Shear Wave Elastography (STL-SWEI) to generate local estimates of axial strain, shear strain, and Shear Wave Speed (SWS). These local values were registered and non-linear elastograms reconstructed with a novel nonlinear shear modulus estimation scheme for general deformations. Results on tissue mimicking phantoms were validated with mechanical measurements and multiphysics simulations for all deformation types with an error in NLSM of 6–13 %. Quantitative performance metrics with the new compound-motion tracking strategy reveal a 10–15 dB improvement in Signal-to-Noise Ratio (SNR) for simple shear versus pure compressive deformation for NLSM elastograms of homogeneous phantoms. Similarly, the Contrast-to-Noise Ratio (CNR) of NLSM elastograms of inclusion phantoms improved by 25–30 % for simple shear over pure uni-axial compression. Our results show that high fidelity NLSM estimates may be obtained at ~ 30 % lower strain under conditions of shear deformation as opposed axial compression. The reduction in strain required could reduce sonographer effort and improve scan safety.

Index Terms—

Acoustoelasticity; quasi-static and shear wave elastography; nonlinear shear modulus; nonlinear elasticity; material nonlinearity; simple shearing; complex tissue motion

---

sgoswam2@ur.rochester.edu.

I. Introduction

Nonlinear elasticity [1]–[6] is a potential biomarker to improve the positive predictive value (*PPV*) of elastographic systems for detecting breast cancer in women. Images of nonlinear modulus offer enhanced contrast [3]–[4] that improves detectability of otherwise clandestine lesions.

The nonlinear elastic properties of soft tissues are apparent on application of large strains. Hall [6], Varghese [7], Oberai *et al.* [8] used quasi-static elastography to determine the slope of the stress-strain curve and produced images of a nonlinear parameter defined as the rate at which the curve departs from linear behavior. This parameter is sensitive to the nature of induced deformation. Hence a single parameter that can explicitly convey quantitative measure of nonlinear shear modulus (NLSM) irrespective of different deformations applied is important. Quantifying nonlinear shear modulus (NLSM) images is difficult with quasi-static elastography [9]–[11] as it requires solving an ill-posed inverse problem. On the other hand, dynamic elastography [12]–[16] readily quantifies linear elastic modulus, but the displacement induced by acoustic radiation force is not large enough to exhibit tissue nonlinearity. These complementary properties suggest the combination of quasi-static elastography with dynamic elastography to measure the strain dependence of shear wave speed, from which we can obtain the NLSM.

Several groups have taken this approach to NLSM imaging. Gennison *et al.* [1] derived constitutive equations from acoustoelastic theory to obtain the NLSM of soft tissues under the influence of uniaxial loading. The acoustoelastic theory has been applied by combining strain elastography and supersonic shear wave imaging [20] to evaluate the nonlinear mechanical properties in tissue mimicking materials [17], breast [18], and kidneys [19]. Axial deformations were tracked and the shear wave speed (*SWS*) were measured under increasing compression to obtain NLSM maps. Our previous article [21] established that local NLSM imaging could be improved by tracking both lateral and axial deformations. The acoustoelastic formulations proposed by Gennison *et al.* [1] to relate shear wave speed to nonlinear elasticity constants is restricted to a Green strain energy function. Rosen *et al.* [22]–[23] evaluated the use of several hyperelastic strain energy functions to represent acoustoelastic shear wave data and investigated the consistency of the nonlinear elastic parameters.

In each of the above approaches, NLSM imaging was performed with uniaxial compression applied to the material. The practical challenges in exerting uniaxial compression during freehand scanning [24] motivates the development of an NLSM imaging method suitable for both lateral and axial deformations.

We present a closed-form solution for NLSM estimation relating the change in SWS for a medium subjected to simple shear deformation. We observed in our previous study that SWS in a medium subjected to simple shear deformation increases [25] with increasing shear strain, which can be attributed to the in-plane normal stresses that hold the medium in its deformed state. The NLSM model is further extended to accommodate compound compressional and shear deformations. The model is most applicable to in-vivo use, since deformations in freehand scanning are seldom purely compressional or shear.

In our expreiments, strain was applied in multiple controlled steps and 2-D cross-correlation search [26]–[27] was used to obtain axial and lateral deformation maps, leading to axial and shear strain maps. SWS maps were obtained by single track location shear wave elasticity imaging (STL-SWEI) [13]-[15] at each deformation step. The slope of the regression line fit to the SWS squared as a function of strain data measurements yields an estimate of the nonlinear shear modulus map.

The article is organized as follows. First, we derive NLSM expressions for pure shearing and for compound motion. The method is tested on tissue mimicking homogeneous and inclusion phantoms. The method is further validated with a mechanical unconfined compression testing and a finite element simulation study. The results are followed with a discussion and conclusion.

II. Theory

Gennisson [1] derived an expression for NLSM of soft tissues from strain energy density functions following uniaxial compression. Landau and Lifshitz [28]–[31] proposed a third order expansion for elastic energy density of an isotropic elastic solid in terms of Lagrangian strain tensor ($u_{i'}$) invariants

$$u_{i'k'} = \frac{1}{2}\left(\frac{\partial u_i}{\partial x_{\widetilde{k'}}} + \frac{\partial u_k}{\partial x_{\widetilde{i'}}} + \frac{\partial u_l}{\partial x_{\widetilde{i'}}}\frac{\partial u_l}{\partial x_{\widetilde{k'}}}\right) \tag{1}$$

where u_i are particle displacement, x_i are Eulerian co-ordinates, $x_{\widetilde{i'}}$ are Lagrangian co-ordinates, and $x_i = x_{\widetilde{i'}} + u_i$. The invariants of strain tensor are defined as:

$$I_1 = tr\{u\} = u_{i'l'}, \quad I_2 = tr\{u^2\} = u_{i'k'}u_{k'i'}, \quad I_3 = tr\{u^3\} = u_{i'k'}u_{k'l'}u_{l'i'} \tag{2}$$

An expansion of the Landau-Lifshitz strain energy density to the third order of strain is

$$\varepsilon = \mu I_2 + \left(\frac{1}{2}K - \frac{1}{3}\mu\right)I_1^2 + \frac{1}{3}AI_3 + BI_1I_2 + \frac{1}{3}CI_1^3 \tag{3}$$

where μ is the shear modulus, K the linear bulk modulus and A, B and C the third-order elastic constants, describing the quadratic nonlinear response of the deformed solid. For an incompressible medium, the strain energy [1], [32], [33] may be expressed in terms of independent invariants I_2, I_3 and $III_u = \rho_0^2/\rho^2$, the third principal invariant of strain deformation tensor. From the Caley-Hamilton theorem, for the strain tensor, we have

$$-\mathbf{u}^3 + I_u\mathbf{u}^2 - II_u\mathbf{u} + III_u\mathbf{I} = 0 \tag{4}$$

where **I** is the identity matrix and

$$I_u = tr\{u\}, II_u = \frac{1}{2}\left[(tr\{u\})^2 - tr\{u^2\}\right], III_u = det\{u\} \tag{5}$$

are principal invariants of **u** which are again related to (2) by

$$I_u = I_1, \quad II_u = \frac{1}{2}\left(I_1^2 - I_2\right), \quad III_u = \frac{1}{6}I_1^3 - \frac{1}{2}I_1 I_2 + \frac{1}{3}I_3 \tag{6}$$

For an incompressible medium $III_u = 1$, and neglecting the fourth order elastic terms under the assumption of only small amplitude plane waves, the strain energy expression in (3) is simplified to

$$\varepsilon = \mu I_2 + \frac{1}{3}AI_3 \tag{7}$$

Landau and Lifshitz [28] obtained the equation of motion in Lagrangian co-ordinates (a, t) defined by

$$\rho_0 \frac{\partial^2 u_i}{\partial t^2} = \frac{\partial \sigma_{ik}}{\partial a_k} \tag{8}$$

where a is equilibrium position of particle, t is the time, ρ_0 is the density of the material in its undeformed state and σ_{ik} is the stress tensor defined by

$$\sigma_{ik} = \frac{\partial \varepsilon}{\partial(\partial u_i / \partial a_k)} \tag{9}$$

Considering linearly polarized plane shear wave propagation and neglecting higher order static deformations (the detailed derivations are provided in Supplementary Materials section 1A), the plane wave equation becomes

$$\rho_0 \frac{\partial^2 u_2^D}{\partial t^2} = \frac{\partial^2 u_2^D}{\partial x_1^2}\left[\mu + 2\mu\left(2\frac{\partial u_1^S}{\partial x_1} + \frac{\partial u_2^S}{\partial x_2}\right) + \frac{A}{2}\left(\frac{\partial u_1^S}{\partial x_1} + \frac{\partial u_2^S}{\partial x_2}\right)\right] \tag{10}$$

where u^S is the static displacement due to simple shearing and u^D the dynamic displacement due to shear wave propagation. The deformation known as simple shear [34] has mathematical representation given by

$$a_1 = x_1 + kx_2, \quad a_2 = x_2, \quad a_3 = x_3, \tag{11}$$

where (x_1, x_2, x_3) and (a_1, a_2, a_3) denote Cartesian coordinates of a particle before and after deformation respectively and $k > 0$ is an arbitrary dimensionless constant called shear strain. The deformation gradient tensor **F**, the left Cauchy-Green strain tensor $\mathbf{B}=\mathbf{FF}^T$ and its inverse are:

$$\mathbf{F} = \begin{bmatrix} 1 & k & 0 \\ 0 & 1 & 0 \\ 0 & 0 & 1 \end{bmatrix}, \quad \mathbf{B} = \begin{bmatrix} 1 + k^2 & k & 0 \\ k & 1 & 0 \\ 0 & 0 & 1 \end{bmatrix}, \quad \text{and} \quad \mathbf{B}^{-1} = \begin{bmatrix} 1 & -k & 0 \\ -k & 1 + k^2 & 0 \\ 0 & 0 & 1 \end{bmatrix} \tag{12}$$

and the three principal invariants of strain tensor are

$$I_u = II_u = 3 + k^2, \quad \text{and} \quad III_u = 1, \tag{13}$$

Combining (6) and (13), we obtain

$$I_1 = 3 + k^2, \quad I_2 = \left(3 + k^2\right)\left(1 + k^2\right), \quad \text{and} \quad I_3 = \frac{3}{2}\left(3 + k^2\right)^2\left(1 + k^2\right) - \frac{1}{2}\left(3 + k^2\right)^3 + 3 \tag{14}$$

The spatial derivatives of the static displacement are

$$\frac{\partial u_1^S}{\partial x_1} = -\frac{T_{11}}{E} = -\frac{T_{11}}{3\mu}, \quad \frac{\partial u_2^S}{\partial x_2} = -\frac{T_{22}}{E} = -\frac{T_{22}}{3\mu} \tag{15}$$

where the in-plane normal stresses are $T_{11} = 2k^2\frac{\partial \varepsilon}{\partial I_u}$ and $T_{22} = -2k^2\frac{\partial \varepsilon}{\partial II_u}$. From nonlinear theory of shear deformation proposed by Rivlin *et al.* [35], an incompressible isotropic homogeneous material following simple shear has normal in-plane stress that hold the material in its deformed state. The strain energy density function can be written in terms of simple shear combining (7) and (14) as

$$\varepsilon = \mu\left(3 + k^2\right)\left(1 + k^2\right) + \frac{A}{3}\left(\frac{3}{2}\left(3 + k^2\right)^2\left(1 + k^2\right) - \frac{1}{2}\left(3 + k^2\right)^3 + 3\right) \tag{16}$$

which gives

$$\frac{\partial \varepsilon}{\partial I_u} = \frac{\partial \varepsilon}{\partial II_u} = 2\mu\left(2 + k^2\right) + A\left(3 + k^2\right)\left(1 + k^2\right), T_{11} = -T_{22} \tag{17}$$

Solving (15 – 17) and (10) the nonlinear elastodynamic equation is rewritten as

$$\rho_0 V_{21}^2 = \mu - \frac{8}{3}\mu k^2\left(k^2 + 2\right) - \frac{4}{3}Ak^2\left(k^2 + 1\right)\left(k^2 + 3\right). \tag{18}$$

Neglecting higher orders of shear strains, the final elastodynamic expression is given by

$$\rho_0 V_{21}^2 = \mu - k^2\left(\frac{16}{3}\mu + 4A\right) \tag{19}$$

with V being the shear wave velocity.

For compound motion having both shear (k) and compression ($c = 1 - a$), the elastodynamic equation is

$$\mu_i = \rho_0 V^2 = \mu - \frac{1}{3\mu}\left(\mu\left(2a^2 + \frac{2}{a}\right) + A\left(a^4 + a + \frac{1}{a^2}\right)\right)$$
$$\left(4k^2a^2\mu + 8a^2\mu - 8a^{-1}\mu + 2a^2A - 2a^{-1}A\right) \tag{20}$$

The detailed derivations of NLSM for compound deformation is given in Supplementary Material section IB.

Note, in (20) for simple shear $a=1$ and (20) reduces to (19). Similarly, for pure compression, the derivatives of static displacements are $\frac{\partial u_2^S}{\partial x_2} = -\frac{T_{22}}{3\mu}$, $\frac{\partial u_1^S}{\partial x_1} = -\frac{T_{22}}{6\mu}$ and (20) reduces to $\rho_0 V_{21}^2 = \mu - \frac{T_{22}}{12\mu}A$ which is Gennisson's acoustoelastic model derived for uniaxial compression case. Further, when the medium is undeformed (k=0, a=1), (20) corresponds to the result for an isotropic linear elastic material ($\rho_0 V^2 = \mu$). Similarly, for the simple shear NLSM expression in (19), when the medium is unstressed, (19) is consistent with classical shear wave propagation equation. Changing the amount of shear (k) in (19) is equivalent to modifying the apparent shear modulus ($\mu_i = \rho_0 V^2$) according to squared dependence of shear strain, initial shear modulus (μ) and third order nonlinear coefficient (A). With change of lateral shear deformation directions from +x to −x, shear strain changes from +k to −k, but the apparent shear modulus according to (19) remains unaffected consistent with physical symmetry. This has been further validated expermentally in Section III and Fig. S6 of Supplementary Materials. Further, if we assume there is no nonlinearity associated with medium when there is compound deformation, the in-plane normal stresses according to [35] do not exist, hence static displacements $\frac{\partial u_1^S}{\partial x_1}$ and $\frac{\partial u_2^S}{\partial x_2}$ in (15) account to zero. The wave equation (10) then reduces to $\rho_0 \frac{\partial^2 u_2^D}{\partial t^2} = \mu \frac{\partial^2 u_2^D}{\partial x_1^2}$, the classical shear wave propagation equation.

In this study, lateral shear strain and axial compressional strain were used. Lateral shear (k) and axial compressional strain (c) maps were estimated from pre-stressed and post-stressed echo data, and simultaneously the shear wave speed (V) map was measured at each compound motion step. From the shear wave speed map, the apparent shear modulus (μ_i) was obtained for each of the motion steps. By fitting in the apparent shear modulus (μ_i), the undeformed state shear modulus (μ), the axial (c) and shear (k) strain in (20), the NLSM (A) was estimated at each motion step.

III. Materials and methods

A. Finite Element Simulation of Nonlinear Shear Modulus

Finite element model (FEM) simulations were performed using the COMSOL Multiphysics 5.2. Homogeneous and inclusion models were meshed using triangular elements. A grid size of 20 mm by 20 mm was generated using a FEM containing 31080 elements. A Mooney-Rivlin model was used to simulate a tissue-like material. The Young's modulus was assumed to be the value measured at zero stress. Poisson's ratio was fixed at 0.499. For compressional deformation, the displacement of the lower face of samples was constrained along vertical axis (y-axis) and allowed to move freely in x-direction. The top surface was displaced in y-direction to give 20% global strain in 30 equivalent steps and allowed to move freely in x-direction. For pure shearing motion, the top surface was constrained along y-axis and displaced by 20% global strain along x-axis. For compound deformation, the top surface of the sample was displaced along the vertical and horizontal axes, replicating compound compression and shearing. The lower surface in this case was constrained along both vertical and horizontal directions. The resulting cumulative vertical axial strain (c), cumulative shear strain (k) and nominal or first Piola-Kirchhoff stress (T) were calculated. The value of A given by the compound motion estimator is related to the nominal stress, cumulative axial and shear strain by the relation :

$$T = \left(4a^2 - 4a^{-1} - 2k^2a^2\right)\left(\mu\left(2k^2a^2 + 2a^2 + \frac{2}{a}\right) + A\left(a + \frac{1}{a^2} + 2ak^2\right)\right), \quad c = 1 - a \tag{21}$$

The detailed derivations of (21) are provided in the Supplementary Materials section IC. The simple shearing NLSM estimator solution relating the stress, differential shear strain and linear shear modulus is given by:

$$T_i = \sum_{j=1}^{i} \mu_j \Delta k_j, \quad \mu_i = \mu_0 - k^2\left(\frac{16}{3}\mu + 4A\right) \tag{22}$$

For compressional NLSM estimator, the stress, axial strain and NLSM A is related by:

$$T_i = \sum_{j=1}^{i} 3\mu_j \Delta c_j, \quad \mu_i = \mu_0 - \left[\sum_{j=1}^{i} 3\mu_j \Delta c_j\right]\frac{A}{12\mu_0} \tag{23}$$

Here, Δk_j and Δc_j were the differential shear and axial strain simulated to get the apparent shear modulus μ_i. The apparent shear modulus and the simulated cumulative strain were used to estimate the NLSM A. Note that nonlinear shear modulus A cannot be obtained directly from COMSOL multiphysics. With the knowledge of the simulated strain, stress outputs and the assumption of the linear shear modulus, (21), (22), and (23) were used to obtain A by compound, shear and compressional estimator, respectively. We used compound NLSM estimator to estimate A in subsequent studies unless otherwise mentioned.

B. Experimental methods and data acquisition

1) Phantoms: We fabricated homogeneous gelatin phantoms from 200-bloom type A (Custom Collagen, Addison, IL) gelatin. The phantoms had a volume 750 ml, with 6–11.5% gelatin concentration, 1% cornstarch for ultrasound scattering, and remaining volume of de-ionized (DI) water. Homogeneous cryogel phantoms were fabricated from a 6–10% polyvinyl alcohol (PVA) solution (molecular weight 44.053 g per mol, J.T.Baker™).

Cylindrical inclusion phantoms were constructed with inclusion of diameter 0.65 cm. Gelatin solution was prepared for the background medium and poured in a mold containing a 6.5 mm diameter aluminium cylinder and allowed to solidify. The cylinder was then removed and gelatin solution for inclusion medium poured into the cylindrical space and allowed to solidify. Simultaneously, cylindrical samples of 2-cm diameter and 3.5-cm height were made for mechanical testing with the same mixture used to make homogeneous samples for ultrasound measurements. For mechanical testing of heterogeneous phantoms, the background gel and inclusion solution were separately used to make two cylindrical samples.

2) Experimental Setup: All imaging experiments were carried out using a ATL L7–4 linear array driven by a Verasonics Vantage 64LE ultrasound system (Verasonics Inc., Kirkland, WA, USA) shown in Fig. 1. A compression plate (9cm × 5.5cm) was attached to the transducer, itself mounted on a 5-axis position controller. Sand paper was applied to the compression plate and table surface to prevent slipping of the phantom under lateral shear. The 5-axis positioner was used to apply axial compression and lateral shear in controlled increments. Data corresponding to 30 progressive deformation steps (up to a total 20% global strain) were collected. Five different deformation types were applied to the phantom, namely, 20% pure compression, 20% lateral simple shearing, an equal compression (20%)-shearing (20%) compound deformation (EC), a high compression (20%) low shearing (10%) compound deformation (HCLS), and a high shearing (20%) low compression (10%) compound deformation (HSLC).

Raw channel data were acquired at a ultrasound frequency of 5 MHz, 60% bandwidth. We acquired data from successive plane wave transmissions at forty different transmission angles between −7° and 7° and used in plane wave compounding [36] to improve lateral motion estimation. Delay-and-sum (DAS) beamforming implemented on a graphics processing unit (GPU) was applied to the raw channel data.

3) Strain Mapping with 2D motion registration: The axial (dz) and lateral (dx) displacements between the pre- and post-motion RF echo frames were estimated using a 2D cross-correlation-based similarity search algorithm [26], [27]. A 2.5 mm× 2.5 mm kernel was applied to track motion between the pre and post-motion echo frames with an overlap of 80% in both axial and lateral directions. This kernel size corresponds to 15 channel lines of RF data laterally and 7–10 wavelengths axially. 2-D spline interpolation was used to calculate the sub-pixel displacements [27]. Note, a total of 20% global strain was applied in 30 equivalent small steps or frames, with 0.66% strain at each step or frame. The displacement estimation procedure was followed at each of these steps and this displacement was small enough to minimize the effects of signal decorrelation caused by larger deformations. The displacements were then accumulated over all the frames and registered with respect to the initial un-deformed state of the medium. The axial strain (c) and shear strain (k) [37] were quantified using first derivative least square strain estimator.

4) SWEI Processing: The single-track location shear wave elasticity imaging (STL-SWEI) sequence consisted of pair of push beams with a common tracking line. With our STL-SWEI implementation, the ensemble of tracking and push beams was translated over the entire field of view (FOV) to form the shear wave image. The distance (ΔP) between push beams was kept constant at 3.5mm and ΔT between left push and track beam was 7.5mm. All STL-SWEI sequences had 30 pairs of push beams to cover an FOV of 21 mm.

The particle displacement versus time at every depth in the region of interest was estimated using 2-D autocorrelation method of Loupas [38]. A tracking pulse repetition frequency of 7kHz was used. The shear wave arrival time difference was estimated from cross-correlation of displacement vs time profile associated with each push pulse. The distance between push beams divided by difference in shear wave arrival times provides the shear wave speed (V_S). The linear shear modulus (μ) is related to V_S by $u = \rho \cdot V_S^2$ where ρ is medium density. For quasi-incompressible soft tissue materials with Poisson's ratio 0.5, the stiffness defined by Young's modulus can be approximated by $E \approx 3\mu$. Then by using (20), a 2-D NLSM map (Fig. 2) is obtained by fitting apparent shear modulus, shear strain and axial strain. The cummulative compressive (T_c) and shear (T_s) stresses were obtained from differential strain times apparent shear modulus (μ_j) at each motion step j as given by:

$$T_{c_i} = \sum_{j=1}^{i} 3\mu_j \Delta c_j, T_{s_i} = \sum_{j=1}^{i} \mu_j \Delta k_j \tag{24}$$

where (Δc_j) and (Δk_j) were the differential axial and shear strain, respectively, measured at each deformation step.

C. Mechanical Measurement of NLSM

Unconfined compression measurement of NLSM [21] was performed to validate our method. Fig. S2a of Supplementary Materials shows the experimental setup of mechanical stress–strain measurement system. A 5N load cell was used to measure applied force, while cylindrical homogeneous phantoms were deformed to obtain the stress–strain curve. The tangent of this curve at zero strain gives us the linear shear modulus. The apparent shear modulus is obtained by taking the tangent of this curve at the given strain level. With the knowledge of the stress, apparent shear modulus and the stress-free shear modulus, NLSM is calculated by curve fitting according to (4 and 5) of [21]. This NLSM has been used to conduct the subsequent studies.

IV. Results

A. Validation of NLSM and comparison with existing methods

Fig. 3a shows stress-strain curve obtained by mechanical uni-axial compression (blue line) and ultrasound measurements of uni-axial compression (red line), simple shearing (yellow) and compound deformation (violet) on a 8 kPa gelatin homogeneous material. Fig. 3b demonstrates bar plot of nonlinear parameter γ used by Oberai *et al.* [8]. γ presents the rate at which stress-strain curve deviates from linear behavior. The difference of nonlinear parameter γ observed between different deformation types is 10–53%. The corresponding NLSM parameter estimated by our compound estimator, shown in barplot of Fig. 3c, gives good agreement with a difference of 6–13% between different deformations. Moreover, compound deformation NLSM estimator gives better results compared to exisiting uniaxial-compression estimator as shown in Fig. 3d.

B. Simulation Results

1) Homogeneous Model: From Fig. 4, it is observed that the NLSM obtained with uniaxial compression deformation has good correspondence with that of simple shearing deformation, with values of 89.2 ± 0.6 kPa, 144.8 ± 1.3 kPa and 89.4 ± 0.5 kPa, 145 ± 1.1 kPa for compression and shearing respectively, for linear shear moduli of 8, 18 kPa. The values were retrieved by taking mean and standard deviation within a window of 5 × 5 mm. These values were consistent with the mechanically obtained NLSM of 91 kPa, 150.2 kPa for linear shear moduli of 8, 18 kPa.

2) Heterogeneous model: Fig. 5 shows the NLSM maps obtained for an inclusion of linear shear modulus 18 kPa in a 8 kPa medium against varying strain levels. The first row represents pure compressional deformation, while the second row represents simple shearing deformation applied to the simulation model. At low strain, NLSM map does not portray the inclusion well, as there is little deviation from linear behaviour. With increasing strain, the estimated NLSM image exhibits good contrast. NLSM values were in good agreement for both compression and shearing, 142 ± 3.7 kPa for simulated compression and 151 ± 1.3 kPa for simulated shearing deformation. These values were obtained by taking mean and standard deviation (SD) within a 4 × 4 mm window for inclusion and 4 × 8 mm for the media.

3) Compound Deformation: High compression compound deformation (HCLS) and high shearing compound deformation (HSLC) were applied in the inclusion simulation model and the corresponding NLSM maps obtained are shown in Fig. 6. The simulated NLSM estimates of the inclusion have good agreement between two deformation methods with NLSM of 137 ± 2.8 kPa and 143 ± 1.8 kPa for HCLS and HSLC deformation types, respectively. Fig. 7 shows normalized NLSM values for different combinations of compression and shearing strain, estimated by compression, shearing and compound NLSM estimator. As expected, the compressional and shear estimators give good results when the deformation matches the respective models. The compound estimator performs well regardless of the combination of shear and compression.

C. Experimental Results

1) NLSM of Homogeneous Phantoms: Fig. 8 shows linear and NLSM maps obtained in homogeneous gelatin and PVA phantoms by simple shearing and pure compression deformations. The NLSM values obtained for shearing deformation were 88 ± 5 kPa and 144.4 ± 7.8 kPa for 8 and 18 kPa linear shear moduli gel phantoms, respectively. The corresponding NLSM values for compressional deformation were 85 ± 9 kPa and 138.4 ± 9.4 kPa. Further, it can be seen that NLSM maps estimated by simple shearing have reduced artifacts compared to pure compression. For PVA materials, the NLSM estimated were 76.4 ± 7.4 kPa, 108.4 ± 8.5 kPa and 78.1 ± 5.9 kPa, 110.1 ± 8.4 kPa with compression and shearing, respectively, for 4.7, 10 kPa linear shear modului. The SD of nonlinear elastograms is comparatively higher for PVA material compared to gelatin as seen from Fig. 8. Additionally, the magnitude of NLSM in Fig. 8 demonstrate that PVA is more nonlinear compared to gelatin material. All the values were obtained by taking mean within a 5 × 5 mm window near the shear wave push focus region.

2) NLSM of heterogenous phantoms: Fig. 9 presents NLSM maps obtained for heterogeneous gelatin phantoms by pure compression and simple shearing at different strain levels. NLSM estimates for the inclusion at final strain level of 12% agree for simple shearing and pure compression, with values of 153.4 ± 6.3 kPa and 141.9 ± 10.3 kPa, respectively. The corresponding estimated values of the surrounding media were 84.2 ± 3.1 kPa and 80.5 ± 3.1 kPa for shearing and compressional deformation, respectively. These values were obtained by taking mean and standard deviation within a 4 × 4 mm window for inclusion and 4 × 8 mm for the media. These values were in good accordance with the expected values from mechanical testing of 150.2 kPa and 91 kPa for the inclusion and the surrounding media respectively and the simulated results of Fig. 5. As in the simulation, experimental NLSM images are noisy at low strain due to the small deviation from linear behaviour and the resulting errors fitting to the NLSM expressions, as well as difficulty in obtaining ideal zero-stress initial conditions.

3) Effect of Strain on NLSM Elastograms: Fig. 10 presents graphs of percentage error of NLSM estimates in six homogeneous gelatin phantoms of different elasticity as a function of global strain. The percentage errors of the experimental NLSM (A_T) were calculated with respect to the true NLSM obtained by mechanical unconfined compression testing (A_M). The expression for % error is given by: $\frac{|(A_T - A_M)|}{A_M}\%$. The graph of % error approaches an asymptotic limit after a 8% shear strain or a 12% compression strain. After that strain level, the NLSM estimates do not change with more strain data points, with the asymptotic value being the final estimated NLSM. The strain level at which the estimates reach to asymptotic value is determined by: $|A_s| < \varepsilon$ where A_s is the slope of the graphs in Fig. 10 at each strain point and ε is the threshold value set to 0.1. For example, considering shearing NLSM curve of 6 kPa phantom in Fig. 10, the slope of the curve at strain levels of 3, 4 and 5 % were near about 2, whereas the slope at 7, 8 and 9 % strain were 0.04 which is less than threshold value of 0.1. Note, NLSM A does not vary with strain. The estimates of NLSM are biased at lower strain due to a lack of sufficient strain data points for fitting, and due to the small deviation from linearity at lower strain.

The % error of NLSM estimates by shearing motion (blue line) reaches asymptotic value at lower strain compared to compressional NLSM (red line). Strains of 6–10% were required for the estimator to reach the final NLSM for simple shearing, compared to 9–15% for pure uniaxial compression, as evident from Fig. 10. The standard deviation (SD) of percentage error of NLSM estimates was estimated from 20 repetitive measurements at each strain level and decreases with increasing deformation. Similar results were obtained in heterogeneous phantoms as illustrated in Fig. 7 with 6–8% strain required for shear and 10–12% for pure compression. For the simulated results of homogeneous and heterogeneous models in Fig. S7 of Supplementary Materials and Fig. 5 respectively, 6–8% strain is sufficient to estimate the simple shearing NLSM, while 12% strain is required to obtain the NLSM in compression.

4) Compound Deformation NLSM.: Fig. 11 shows the NLSM maps obtained using the shear, compression, and compound NLSM estimators under two compound deformation conditions: HSLC (20% shear, 10% compression) and HCLS (20% compression, 10%

Author Manuscript

Author Manuscript

Author Manuscript

shear). The NLSM map obtained by compound estimator reflects the inclusion structure better compared to NLSM estimated by simple shear expression and significantly better compared to pure compression expression for HSLC deformation. Similarly, for HCLS deformation NLSM maps obtained by compound and pure compression expressions were comparable, but inclusion shape was distorted in NLSM estimated by simple shear estimator.

Fig. 12 plots the NLSM across a lateral cross-section of the heterogeneous phantoms for four different deformation types estimated by three NLSM expression solutions. The cross-section region was chosen based on the push beam focal region for SWS estimates. The dotted line in the graph presents the true position of the inclusion boundary determined from B-mode image. For higher shearing compound deformation (HSLC), the shearing NLSM (red line) and compound NLSM (blue line) solutions give similar NLSM estimates at true inclusion boundary, while the NLSM estimated by compressional solution is underestimated at the inclusion boundary region. The inclusion is not properly reconstructed as the shear deformation is not modelled in the compressional NLSM estimator. Similarly, for HCLS deformation, the compressional and compound NLSM solution have good agreement, with the compound NLSM having a sharp reconstructed inclusion edge compared to the compressional NLSM. The Contrast to Noise Ratio (CNR) [15], [21] was computed as $CNR = \frac{|\mu_I - \mu_B|}{\sqrt{S_I^2 + S_B^2}}$ where μ_I and S_I are the mean and standard deviation of the NLSM of the inclusion, and μ_B and S_B are the corresponding values for the background. The CNR was calculated using a rectangular window of 3 × 3 mm for both the inclusion and the background. The background window was selected on the left hand side of the inclusion. CNR obtained with the compound NLSM expression under simple shearing deformation was 30%, 15% and 23% higher than for pure compression, HSLC and HCLS compound deformations. The CNR of elastograms obtained with the compound NLSM expression was 20% and 35% higher than simple shearing NLSM solution and 40% and 24% than compressional NLSM solution for HSLC and HCLS compound deformation. This suggests that to obtain higher fidelity NLSM estimates, one should seek to induce as much shear as practical, while using the compound motion solution for NLSM image formation.

Signal to Noise Ratios (SNR) of NLSM estimates in homogeneous phantoms with respect to linear modulus, deformation type and estimator type are shown in Fig. 13. SNR was computed as $SNR = \frac{\mu}{S}$, where μ and S denote the mean and standard deviation of estimated NLSM values in a 5 × 5 mm rectangular window near the push beam focus. In Fig. 13a, the SNR obtained using the compound motion estimator is shown for each of the eight phantoms under four different loading conditions. The highest SNR obtained with the compound deformation estimator (Fig. 13a) was achieved using pure shear deformation, with improvement of 18–24% compared to pure compression, 30–35% compared to HCLS, and 18–20% for HSLC deformation conditions.

For EC compound deformation (20% shear / 20% compression) the SNR’s of NLSM images produced using the compound motion estimator are 35–50% higher compared to those obtained by simple shearing estimator, and 38–52% higher than the pure compression estimator, as shown in Fig. 13b. For simple shearing deformation, SNR obtained by compound and shearing NLSM estimators have good correspondence, as shown in Fig. 13c, while the mismatched pure compression estimator shows significantly worse SNR.

V. Discussion

In this study, we present a new technique with shear induced nonlinear elasticity imaging in phantoms. Most other tissue nonlinearity estimation techniques rely on the slope of the stress-strain curve to detremine the nonlinear parameter, such as, the previously reported parameter γ in [8]. The slope of stress-strain curve for a material depends on the type of deformations, as seen from Fig. 3a. We note that, as shown in Fig. 3b and Fig. 3c, our nonlinear parameter NLSM agrees between different deformation types, whereas the parameter γ varies with deformation types. Additionally, compared to our previous uni-axial compression NLSM estimator, our compound deformation NLSM estimator gives reduced error of 5–13% vs 10–55% for different deformations. The errors were obtained with reference to the true values obtained by the mechanical unconfined compression testing.

NLSM with shearing deformation produced elastograms with 31–47.4% lower spatial standard deviation than compressional NLSM, as shown in heterogeneous phantom results of Fig. 9. This may be partly due to out-of-plane deformations caused by compressional motion, while for simple shearing motion there is only in-plane deformation. The proposed method requires accurate tracking of the scatterers at multiple deformation levels to a reference frame [21]. Echo decorrelation associated with large out-of-plane motion reduces the accuracy of tissue strain estimates and, in turn, NLSM. In this work, we applied deformations to the phantoms using a precisely-controlled translational stage with five degrees of freedom. Consequently, it was possible to minimize out-of-pane motion and maintain speckle correlation over strains up to 20%. Although the applied strain is comparable to previously published studies with similar experimental settings (15% in [18], 30% in [19]), during free-hand in vivo imaging, out-of-plane motion may potentially limit the maximum strain that can be applied to the tissue. Despite this limitation, the results in this study (Fig. 10) indicate that, with shearing deformation, stable estimates of NLSM could be achieved at only 6–8% strain while compressional strain required 10–12% strain to achieve similar estimates. Thus, the shearing based method may be better-suited for free-hand imaging. An alternative solution to out-of-plane motion challenges can be achieved by evaluating the tissue motion in 3D [39]. However, performing SWE in 3D is challenging with conventional ultrasound systems [44]. A slip-free rigid boundary has been assumed while deforming the tissue, which is difficult to mimic experimentally. A robot assisted ultrasound screening system [40], [41] has been developed that will prevent tissue slipping and maintain controlled deformation. Another observation from Fig. 5 and Fig. 9 was that NLSM estimates were obtained at much lower strain for simple shearing compared to uniaxial compression. This may be related to the presence of added normal in-plane stresses T_{11}, T_{22} (shown in section II) in simple shearing, as proposed by Rivlin *et al.* [35]. For simple shearing deformation, the external shear stress adds to the normal in-plane stress, whereas for uni-axial compression, there is the presence of in-plane stress alone.

The simulations presented here do not include the effects of noise or ultrasound tracking but rather focused on comparison of the new models with the earlier compressional model. We plan to include these effects in future work to understand the sources of variances. We did not simulate the dynamic shear wave propagation, rather simulated the static stress distribution following model deformation and thereby estimated the NLSM. While for experimental studies, dynamic shear wave propagation is measured with gradual deformation of phantoms to form the NLSM image. Thus there is a discrepancy between the results of phantom experiments and simulations. Nevertheless, the absolute values of simulated NLSM elastograms provide good agreement with experimental elastograms, with an error in NLSM of 6–13% for homogeneous phantoms and 6–14.3% for inhomogeneous phantoms depending upon the deformations employed. The simulated NLSM elastograms have artifacts towards the sides (Fig. 5 and Fig. 6). This is because boundary condition affects first Piola-kirchoff stress distribution at the sides. These artifacts could be reduced with larger size of the background compared to the inclusion, as illustrated in Fig. S3 of Supplementary Materials. However, the value of the estimated NLSM in the central portion of the elastogram was consistent for all the representative images. (Fig. S3 of Supplementary Materials).

In comparing the experimental and simulated compression results in Fig. 5 and Fig. 9, we observe that experimental NLSM were obtained at lower strain than simulated NLSM. This is likely due to the initial compression given with the compressional plate to ensure it was in contact with the tissue. Ideal zero stress initial condition for compressional deformation was difficult to execute. For simple shearing deformation, there was no initial shearing stress given. Thus simulated and experimental NLSM have good consistency with nonlinearity being estimated at roughly the same strain level of 6–8%.

For hand-held scanning, compound deformation comprising both shear and compression is a more realistic model compared to pure compression and simple shearing. The compound deformation estimator solution for NLSM showed better reconstruction of the inclusion structure and better CNR than simple shearing and pure compression expression in Fig. 11 and Fig. 12. Thus while estimating NLSM, the medium should be deformed by simple shearing as much as possible, followed by reconstruction with compound deformation estimator solution. The method has the ability to detect inclusions as small as 4.6 mm diameter. The effect of inclusion sizes on NLSM images has been shown in Fig. S5 of Supplementary Materials.

Limitations of the method proposed here include high computational expense for compound NLSM reconstruction. The computation time of compound deformation NLSM estimator is 120–130 seconds compared to 50–60 seconds for compression or shear NLSM estimator. Future work will be directed towards improving resolution and accuracy of the nonlinear elastograms with improved lateral tracking [42], [43]. We plan to investigate the effects of improved lateral tracking by interpolation on radio frequency signals or cross correlation function or both on the NLSM elastograms. As quasi-staic and shear wave elastograms have separate image resolutions, we need to explore more into tracking of strain images and combining them with local shear wave speed images to acquire high-resolution NLSM map. In this work, we have utilized STL-SWEI to enable high spatial resolution in linear shear modulus images [45]. Although our implementation of STL-SWEI has a relatively long acquisition duration, it may be possible to increase the push-beam frame rate and acquire data within less than a sec. The feasibility and tissue heating safety of such sequences are already well established [46]. Further, MTL-SWEI imaging sequences can also be used to image in-vivo tissues to have high frame rates.

The finite element software (COMSOL Multiphysics) used here to simulate the stress-strain behavior of nonlinear material model does not allow the nonlinear shear modulus (*NLSM*) to be specified explicitly. The simulated stress and strain values are applied to (21) to produce the NLSM map. Latorre-Ossa *et al.* [17] has also simulated the stress-strain maps to compare with the experimentally accumulated stress, however the NLSM was not simulated. In our study, the simulated and experimental stress estimates were not compared. Instead, the NLSM parameter was chosen for comparison and evaluation, due to the varying stress-strain behavior with different deformations applied as shown in Fig. 3a. However, NLSM estimates are expected to be the same, regardless of the deformations applied. Since the NLSM parameter cannot be explicitly specified, error analysis cannot be performed. However, the NLSM computed from simulated stress-strain, gives good agreement (Fig. 5 and Fig. 6) between different deformations applied to the simulation model. Further the estimates obtained from the simulation studies have good correspondence with the ultrasound measurements and mechanically obtained NLSM. This verifies that compound deformation NLSM estimator reduces the difference in estimates between different deformations.

VI. Conclusion

We have introduced a novel nonlinear shear modulus imaging technique applicable to a range of deformations of tissue. This approach addresses challenges involving quantitative NLSM imaging methods limited to uniaxial compression. Theoretical derivations of NLSM for different motion types were shown and validated for compression, simple shearing, and compound motion schemes. The compound estimator NLSM reduces bias to 5–13% for different deformations applied. Results from inclusion phantoms show that applying NLSM to compound motion reconstruct 2-D nonlinear elastograms and provide high contrast between inclusion and background compared to linear elastograms. CNR is significantly improved by using the compound motion estimator compared to pure compressional and simple shearing NLSM estimators. Furthermore, application of simple shearing resulted in qualitatively and quantiatively better nonlinear elastograms and required small strains compared to other deformations.

Supplementary Material

Refer to Web version on PubMed Central for supplementary material.

Acknowledgments

This work was supported by Office of the Assistant Secretary of Defense for Health Affairs through Breast Cancer Research Program under Award No. W81XWH-17-1-0021 and also in part by NIH grant 5R21EB017503-02.

References

[1]. Gennisson J-L, Catheline S, Bari C, Bercoff J, Tanter M, and Fink M, “Acoustoelasticity in soft solids: Assessment of the nonlinear shear modulus with the acoustic radiation force,” J. Acoust. Soc. Am, vol. 122 no. 6 pp. 3211–3219, 2007. [PubMed: 18247733]

[2]. Duck Francis A., “Nonlinear acoustics in diagnostic ultrasound.,” Ultrasound Med. Biol, vol. 28, no. 1, pp. 1–18,2002. [PubMed: 11879947]

[3]. Erkamp RQ, Emelianov SY, Skovoroda AR, and MO’Donnell, “Nonlinear elasticity imaging: Theory and phantom study,” IEEE Trans. Ultrason., Ferroelectr. Freq. Control, vol. 51(no. 5):532–539, 5 2004. [PubMed: 15217231]

[4]. Krouskop TA, Wheeler TM, Kallel F, Garra BS, and Hall T, “Elastic moduli of breast and prostate tissues under compression,” Ultrason. Imag, vol. 20, no. 4, pp. 260–274, 1998.

[5]. Ogden RW, “Non-Linear Elastic Deformations,” Courier Corporation, 1997.

[6]. Hall TJ, Barboneg PE, Oberai AA, Jiang J, Dord JF, Goenezen S, and Fisher TG, “Recent results in nonlinear strain and modulus imaging,” Current Medical Imaging Reviews, vol. 7, no. 4, pp. 313–327, 2011. [PubMed: 22754425]

[7]. Varghese T, and Ophir J, and Krouskop TA, “Nonlinear stress-strain relationships in tissue and their effect on the contrast-to-noise ratio in elastograms,” Ultrasound Med. Biol, vol. 26, no. 5, pp. 839–851, 2000. [PubMed: 10942831]

[8]. Oberai AA, Gokhale NH, Goenezen S, Barbone PE, Hall TJ, Sommer AM, and Jiang J, “Linear and nonlinear elasticity imaging of soft tissue in vivo: demonstration of feasibility,” Physics in Medicine & Biology, vol. 54, no. 5, pp. 1191, 2009. [PubMed: 19182325]

[9]. Ophir J, Céspedes I, Ponnekanti H, Yazdi Y, and Li X, “Elastography: A quantitative method for imaging the elasticity of biological tissues,” Ultrasonic Imaging, vol. 13, no. 2, pp. 111–134, 1991. [PubMed: 1858217]

[10]. Fatemi M, and Greenleaf JF, “Ultrasound-stimulated vibro-acous-tic spectrography” Science, vol. 280 no. 5360 pp. 82–85, 1998. [PubMed: 9525861]

[11]. Doyley MM “Model-based elastography: A survey of approaches to the inverse elasticity problem,” Phys. Med. Biol, vol. 57 no. 3 pp. R35, 1. 2012. [PubMed: 22222839]

[12]. Nightingale K, McAleavey S and Trahey G, “Shear-wave generation using acoustic radiation force: In vivo and ex vivo results,” Ultrasound Med. Biol, vol. 29, no. 12, pp. 1715–1723,2003. [PubMed: 14698339]

[13]. McAleavey SA, Menon M, and Orszulak J, “Shear-modulus estimation by application of spatially-modulated impulsive acoustic radiation force,” Ultrasonic Imaging., vol. 29, no. 2, pp. 87–104,2007. [PubMed: 17679324]

[14]. Elegbe E, and McAleavey SA, “Single tracking location methods suppress speckle noise in shear wave velocity estimation,” Ultrasonic Imaging., vol. 35, no. 2, pp. 109–125,2013. [PubMed: 23493611]

[15]. Ahmed R, Gerber S, McAleavey SA, Schifitto G, and Doyley M, “Plane wave imaging improves single track location shear wave elasticity imaging,” IEEE Trans. Ultrason., Ferroelectr., Freq. Control, vol. 65, no. 8, pp. 1402–1414, 8. 2018. [PubMed: 29993543]

[16]. Mehrmohammadi M, Song P, Meixner DD, Fazzio RT, Chen S, Greenleaf JF, Fatemi M, and Alizad A, “Comb-push ultrasound shear elastography (CUSE) for evaluation of thyroid nodules: Preliminary in vivo results,” IEEE transactions on medical imaging, vol. 34, no. 1, pp. 97–106, 2015. [PubMed: 25122532]

[17]. Latorre-Ossa H, Gennisson J-L, De Brosses E, and Tanter M, “Quantitative imaging of nonlinear shear modulus by combining static elastography and shear wave elastography,” IEEE Trans. Ultrason., Ferroelect., Freq. Control, vol. 59, no. 4, pp. 833–839, 4. 2012.

[18]. Bernal M, Chamming’s F, Couade M, Bercoff J, Tanter M, and Gennisson J-L, “In vivo quantification of the nonlinear shear modulus in breast lesions: Feasibility study,” IEEE Trans. Ultrason., Ferroelect., Freq. Control, vol. 63, no. 1, pp. 101–109, 1. 2016.

[19]. Aristizabal S, Carrascal CA, Nenadic IZ, Greenleaf JF, and Urban MW, “Application of Acoustoelasticity to Evaluate Nonlinear Modulus inEx VivoKidneys,” IEEE transactions on ultrasonics, ferroelectrics, and frequency control, vol. 65, no. 2, pp 188–200, 2017.

[20]. Bercoff J, Tanter M, and Fink M, “Supersonic shear imaging: a new technique for soft tissue elasticity mapping,” IEEE Trans. Ultrason., Ferroelectr., Freq. Control, vol. 51, no. 4, pp. 396–409,2004. [PubMed: 15139541]

[21]. Goswami S, Ahmed R, Doyley MM, and McAleavey SA, “Non-linear Shear Modulus Estimation with Bi-axial Motion Registered Local Strain,” IEEE Trans. Ultrason., Ferroelect., Freq. Control, vol. 66, no. 8, pp. 1292–1303, 8. 2019.

[22]. Rosen DP, and Jiang J, “A comparison of hyperelastic constitutive models applicable to shear wave elastography (SWE) data in tissue-mimicking materials”, Physics in Medicine & Biology, vol. 64, no. 5, pp 055014, 2019. [PubMed: 30673637]

[23]. Rosen D, and Jiang J, “Analyzing acoustoelastic effect of shear wave elastography data for perfused and hydrated soft tissues using a macromolecular network inspired model,” Journal of biomechanics, vol. 97, pp. 109370, 2019. [PubMed: 31606128]

[24]. Sigrist RM, Liau J, El Kaffas A, Chammas MC, and Willmann JK, “Ultrasound Elastography: Review of Techniques and Clinical Applications,” Theranostics, vol. 7, no. 5, pp. 1303–1329, 2017. [PubMed: 28435467]

[25]. Goswami S, Khan S, Ahmed R, Doyley MM, and McAleavey SA, “Deformation Independent Non-linearity Estimation: Studies and Implementation in Ultrasound Shear Wave Elastography,” 2019 IEEE International Ultrasonics Symposium (IUS), pp. 217–220. IEEE, 2019.

[26]. Korshunov VA, Wang H, Ahmed R, Mickelsen DM, Zhou Q, Yan C, and Doyley MM, “Model-based vascular elastography improves the detection of flow-induced carotid artery remodeling in mice,” Scientific reports, Nature Publishing group, vol. 7, no. 1, PP. 12081, 2. 2017.

[27]. Nayak R, Schifitto G, and Doyley MM, “Noninvasive carotid artery elastography using multielement synthetic aperture imaging: Phantom and Invivo evaluation,” American Assoc. of Phys. Med, vol. 44, no. 8 pp. 4068–4082 5. 2017.

[28]. Landau LD, Kosevich AM, Pitaevskii LP, and Lifshitz EM, “Theory of Elasticity,” Oxford, U.K.:Butterworth-Heinemann, 2002.

[29]. Hughes DS, and Kelly JL, “Second-Order Elastic Deformation of Solids,” Physical review, vol. 92, no. 5, pp. 1145, 1953.

[30]. Norris AN, Hamilton MF, Blackstock DT, “Finite amplitude waves in solids”, Nonlinear Acoustics, Boston, MA, USA:Academic, 1998

[31]. Murnaghan FD, “Finite Deformations of an Elastic Solid,” American Journal of Mathematics, vol. 59, no. 2, pp. 235–260, 1937.

[32]. Hamilton MF, and Blackstock DT, “Non-Linear Acoustics,” New York, NY, USA:Academic, 1998.

[33]. Hamilton MF, Ilinskii YA, and Zabolotskaya EA, “Separation of compressibility and shear deformation in the elastic energy density (L)”, J. Acoust. Soc. Am, vol. 116, no. 1, pp. 41–44, 2004.

[34]. Horgan CO, and Murphy JG, “Simple shearing of soft biological tissues,” Proc. of the Royal Society A: Mathematical, Physical and Engg. Sciences, vol. 467, no. 2127, pp. 760–777, 2010.

[35]. Rivlin RS, “Large elastic deformations of isotropic materials IV. Further developments of the general theory,” Phil. Trans. Royal Soc. London. Series A, Mathematical and Physical Sciences, vol. 241, no. 835, pp. 379–397, 1948.

[36]. Montaldo G, Tanter M, Bercoff J, Benech N, and Fink M, ““Coherent plane-wave compounding for very high frame rate ultrasonography and transient elastography,” IEEE Trans. Ultrason., Ferroelectr., Freq. Control, vol. 56, no. 3, pp. 489–506, 2009. [PubMed: 19411209]

[37]. Rao M, Varghese T, and Madsen EL, “Shear strain imaging using shear deformations,” Medical physics vol. 35, no. 2, pp. 412–423, 2008. [PubMed: 18383661]

[38]. Loupas T, Powers J, and Gill RW, “An axial velocity estimator for ultrasound blood flow imaging based on a full evaluation of the Doppler equation by means of a two-dimensional autocorrelation approach,” IEEE Trans. Ultrason. Ferroelectr. Freq. Control, vol. 42 no. 4, pp. 672–688, 1995.

[39]. Wang Y, Jiang J, and Hall TJ, “A 3-D region-growing motion-tracking method for ultrasound elasticity imaging,” Ultrasound Med. Biol, vol. 44, no. 8, pp. 1638–1653, 2018 [PubMed: 29784436]

[40]. Napoli ME, Freitas C, Goswami S, McAleavey S, Doyley M and Howard TM, "Hybrid Force/Velocity Control With Compliance Estimation via Strain Elastography for Robot Assisted Ultrasound Screening," 7th IEEE International Conference on Biomedical Robotics and Biomechatronics (Biorob), Enschede, 2018, pp. 1266–1273.

[41]. Napoli ME, Goswami S, McAleavey S, Doyley M, and Howard TM, "Probabilistic Mapping of Tissue Elasticity for Robot-Assisted Medical Ultrasound," International Symposium on Robotics Research, 10. 2019, forthcoming.

[42]. Luo J, and Konofagou EE, "A fast normalized cross-correlation calculation method for motion estimation," IEEE transactions on ultrasonics, ferroelectrics, and frequency control, vol. 57, no. 6, pp 1347–1357, 2010.

[43]. Liu Z, Huang C, and Luo J, "A systematic investigation of lateral estimation using various interpolation approaches in conventional ultrasound imaging," IEEE transactions on ultrasonics, ferroelectrics, and frequency control, vol 64, no. 8, pp 1149–1160, 2017.

[44]. Youk JH, Gweon HM, Son EJ, Chung J, Kim JA, and Kim EK, "Three-dimensional shear-wave elastography for differentiating benign and malignant breast lesions: comparison with two-dimensional shear-wave elastography," European radiology vol. 23, no. 6, pp. 1519–1527, 2013. [PubMed: 23212276]

[45]. Hollender PJ, Rosenzweig SJ, Nightingale KR, and Trahey GE, "Single- and multiple-track-location shear wave and acoustic radiation force impulse imaging: Matched comparison of contrast, contrast-to noise ratio and resolution," Ultrasound Med. Biol, vol. 41, no. 4, pp. 1043–1057, 2015. [PubMed: 25701531]

[46]. Fahey BJ, Nightingale KR, Nelson RC, Palmeri ML, and Trahey GE, "Acoustic radiation force impulse imaging of the abdomen: demonstration of feasibility and utility," Ultrasound Med. Biol, vol. 31, no. 9, pp. 1185–1198, 2015.

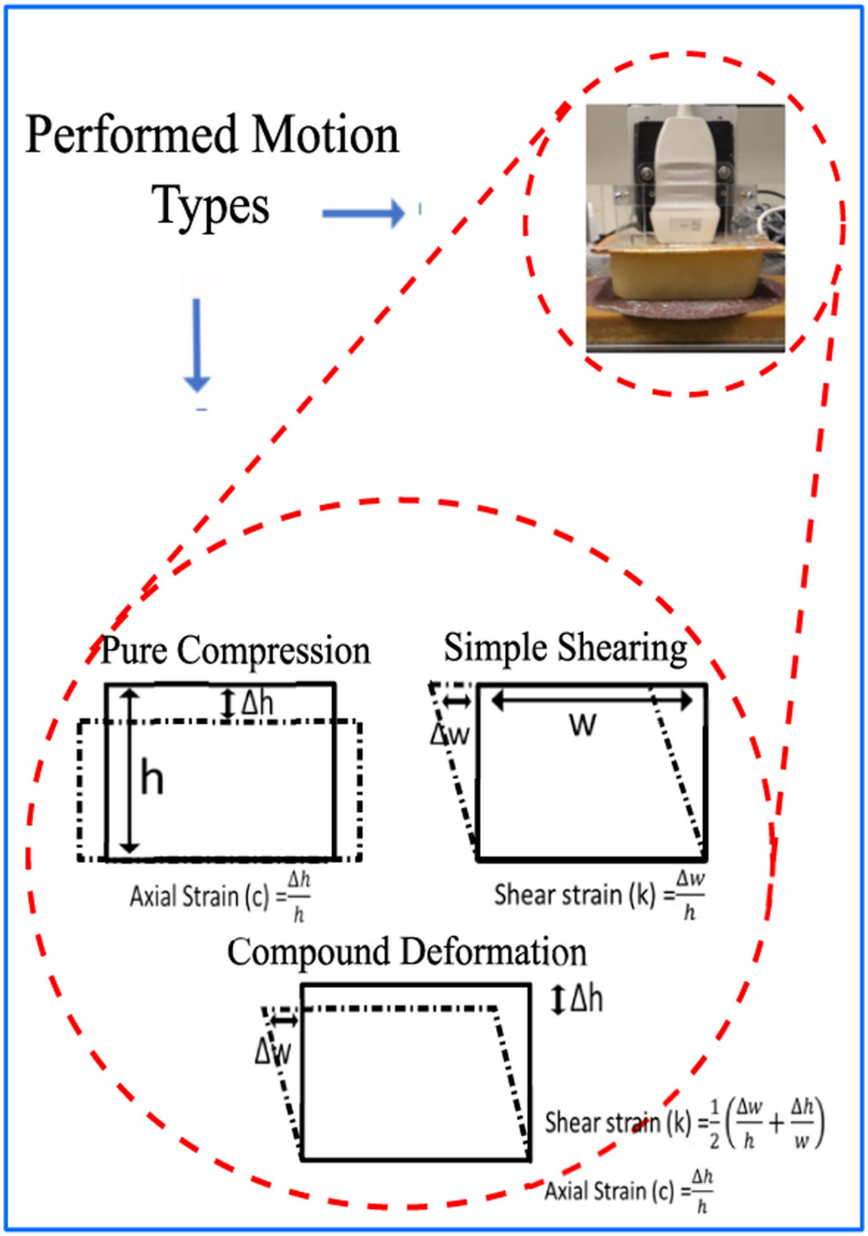

Fig. 1.

Experimental setup for NLSM imaging. A compression plate attached to the transducer. Two sand papers, one in between plate and tissue and one at the bottoms ensures no slipping condition.

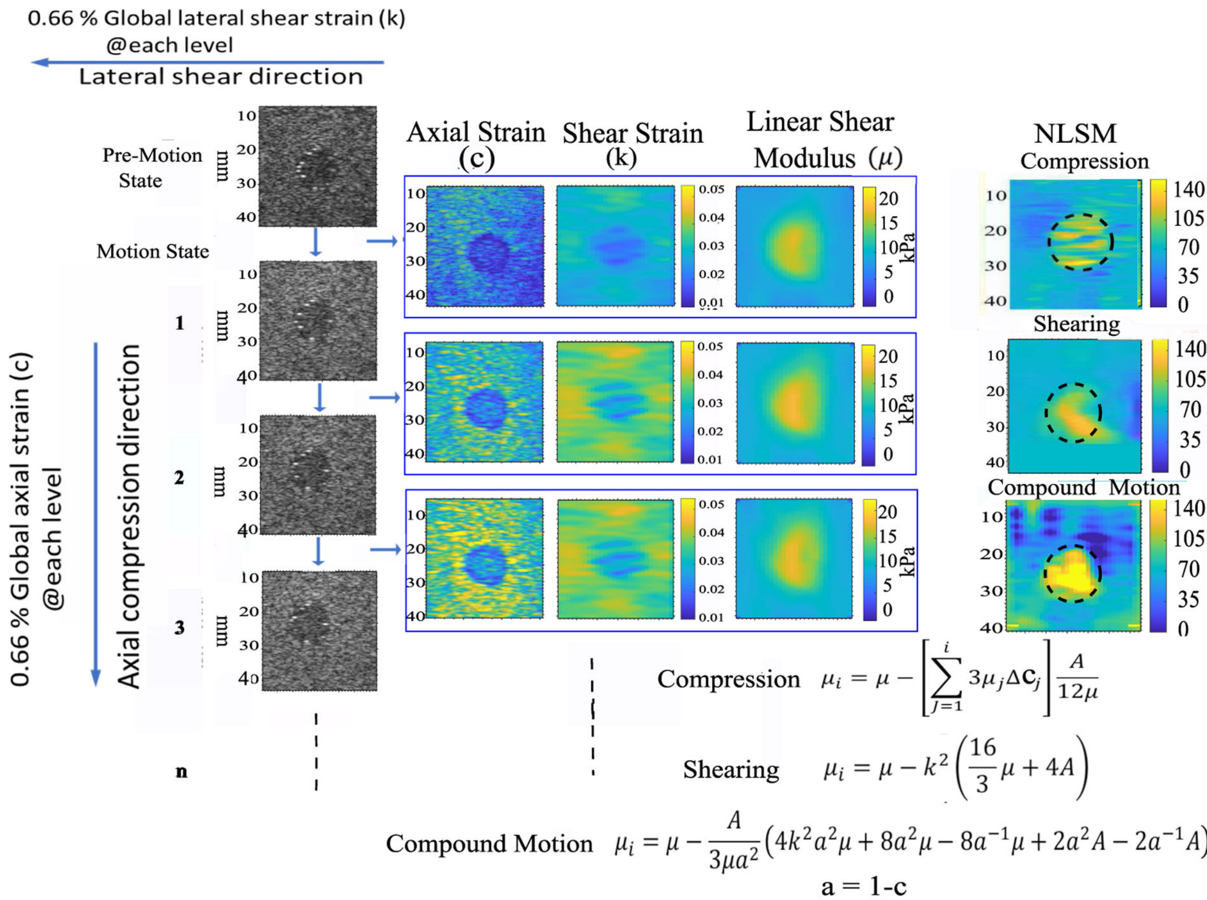

Fig. 2.

Flow diagram showing Nonlinear Shear Modulus Imaging technique with three different NLSM estimators for given compound deformation on an inclusion phantom.

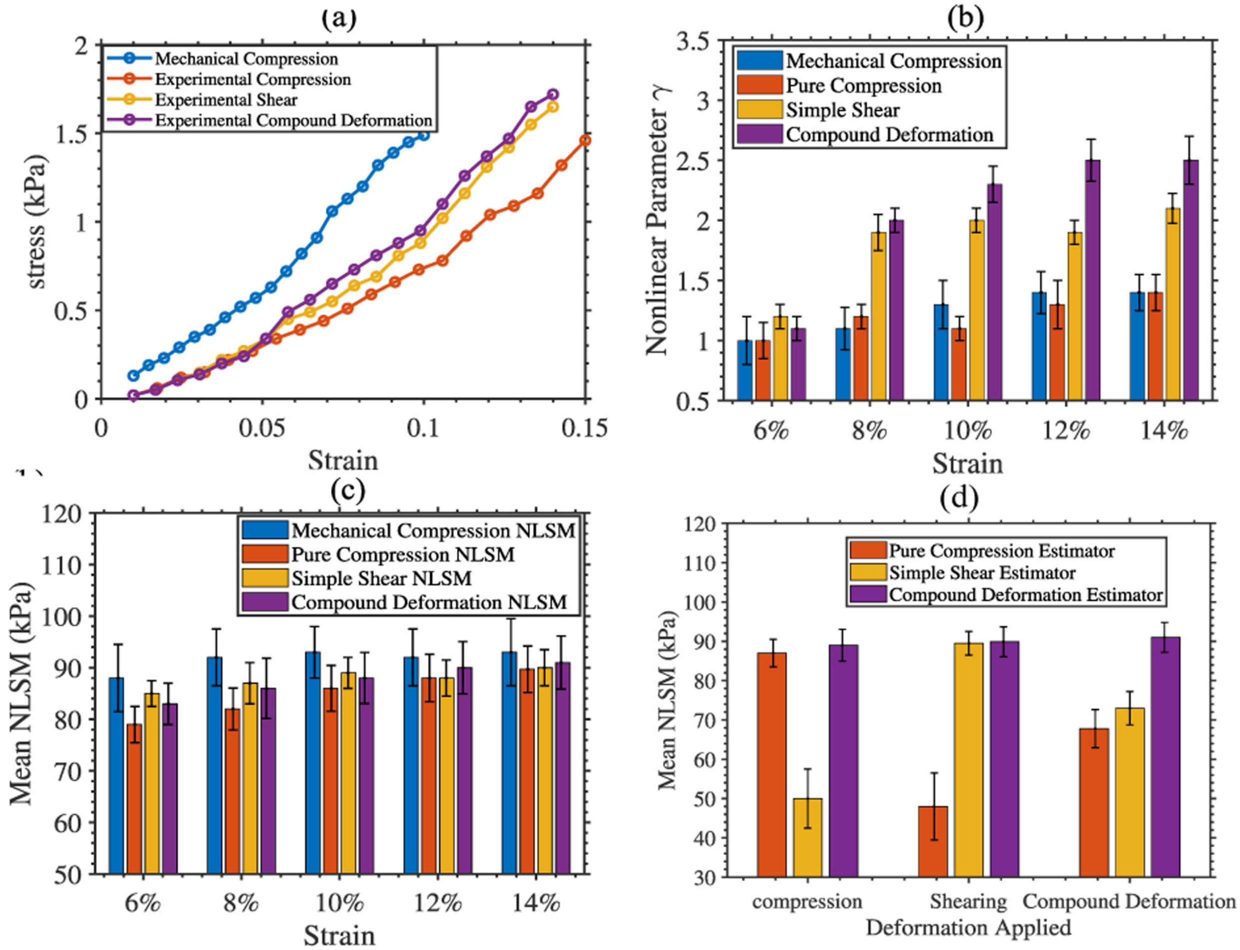

Fig. 3.

(a) Plot showing stress-strain curve for a 8 kPa gelatin material obtained by mechanical measurements of uni-axial compression, ultrasound measurements of uni-axial compression, shearing and equal compound deformation (EC). (b) Nonlinear elasticity evaluated by parameter γ [8]. (c) NLSM evaluated by our compound deformation estimator solution for different deformations. (d) NLSM estimated by uniaxial-compression, shearing and compound estimator solution models. In this case, x-axis shows the three deformations applied.

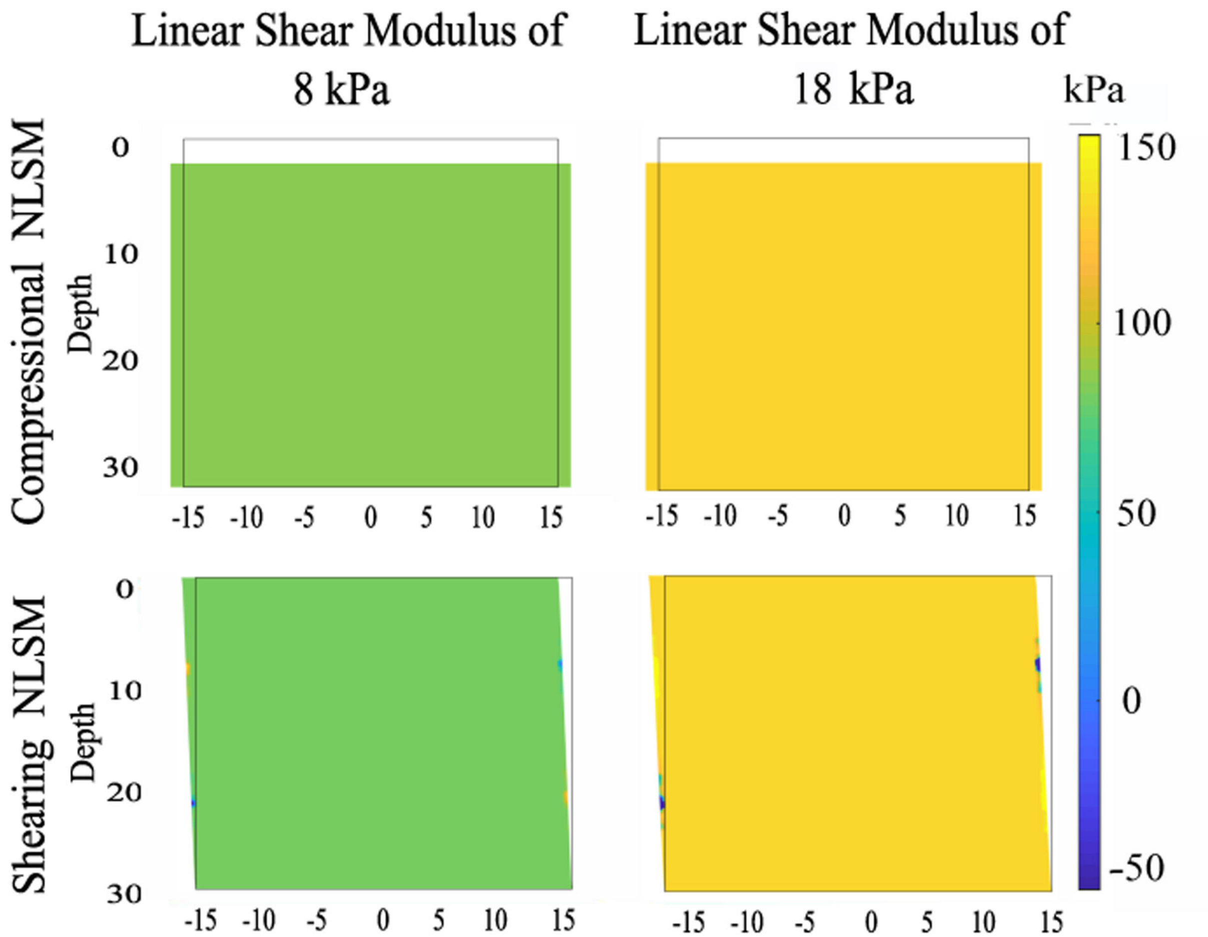

Fig. 4.
Simulated NLSM map by pure compression and simple shearing.

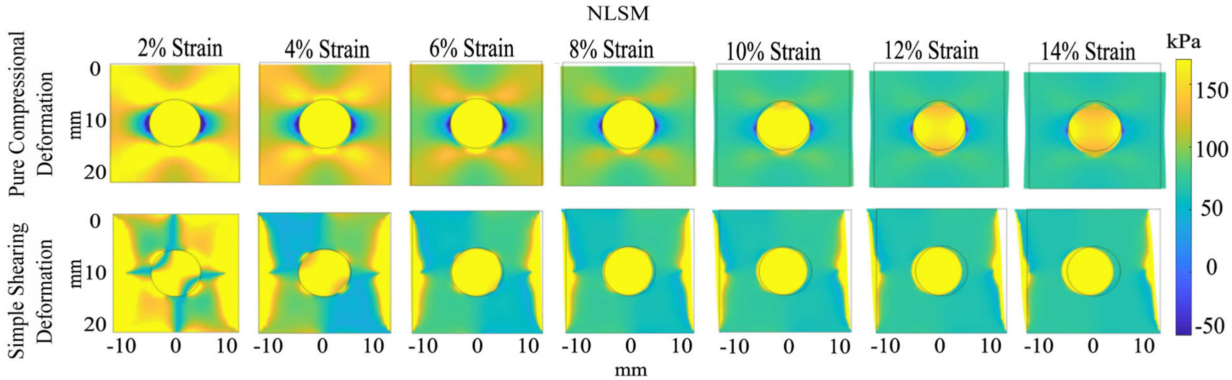

Fig. 5.

Simulated NLSM map by pure compression and simple shearing at different strain levels for a 18 kPa inclusion in 8 kPa medium. The circle represents the original inclusion position.

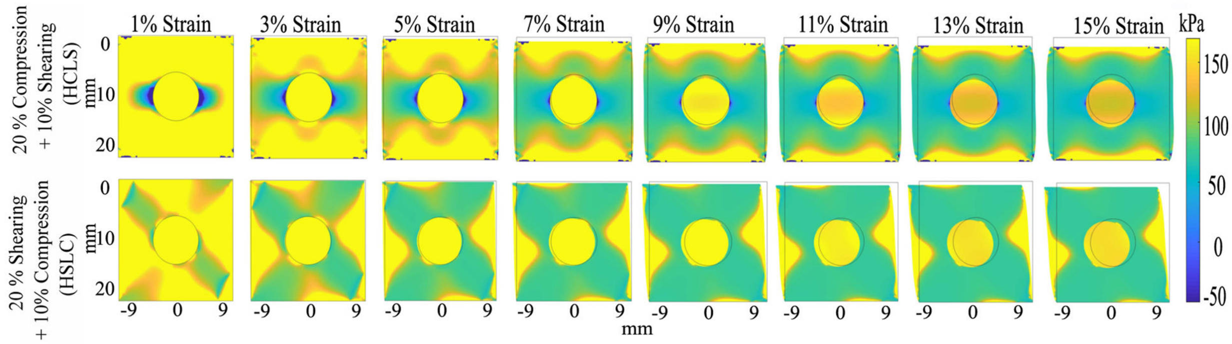

Fig. 6.

Simulated NLSM maps by two types of compound deformation, 20% compression with 10% shearing (HCLS) and 20% shearing with 10% compression (HSLC) for a 18 kPa inclusion in 8kPa medium. The circle represents original inclusion position.

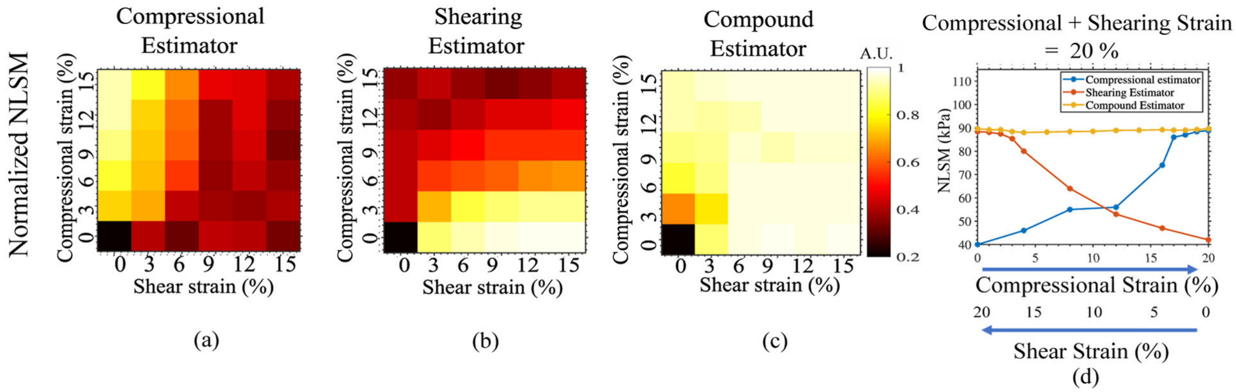

Fig. 7.

Normalized mean NLSM vs compression and shear strain obtained from simulated studies by (a) compressional, (b) shear, and (c) compound NLSM estimator. Values of 1 indicate correct estimation of NLSM, whereas values away from 1 indicate poor NLSM estimation. Simple shearing deformation followed by shearing estimator solution in last row of (b) gives NLSM estimates at lower strain compared to pure compressional deformation followed by compressional estimator solution in 1st column of (a). In (d) the simulated mean NLSM obtained by the three estimators is plotted when the total strain is kept fixed at 20%. In contrast to the shear and compression estimators, the compound estimator gives constant values for all shear/compression combinations. The mechanical NLSM obtained for this phantom is 90.5 kPa.

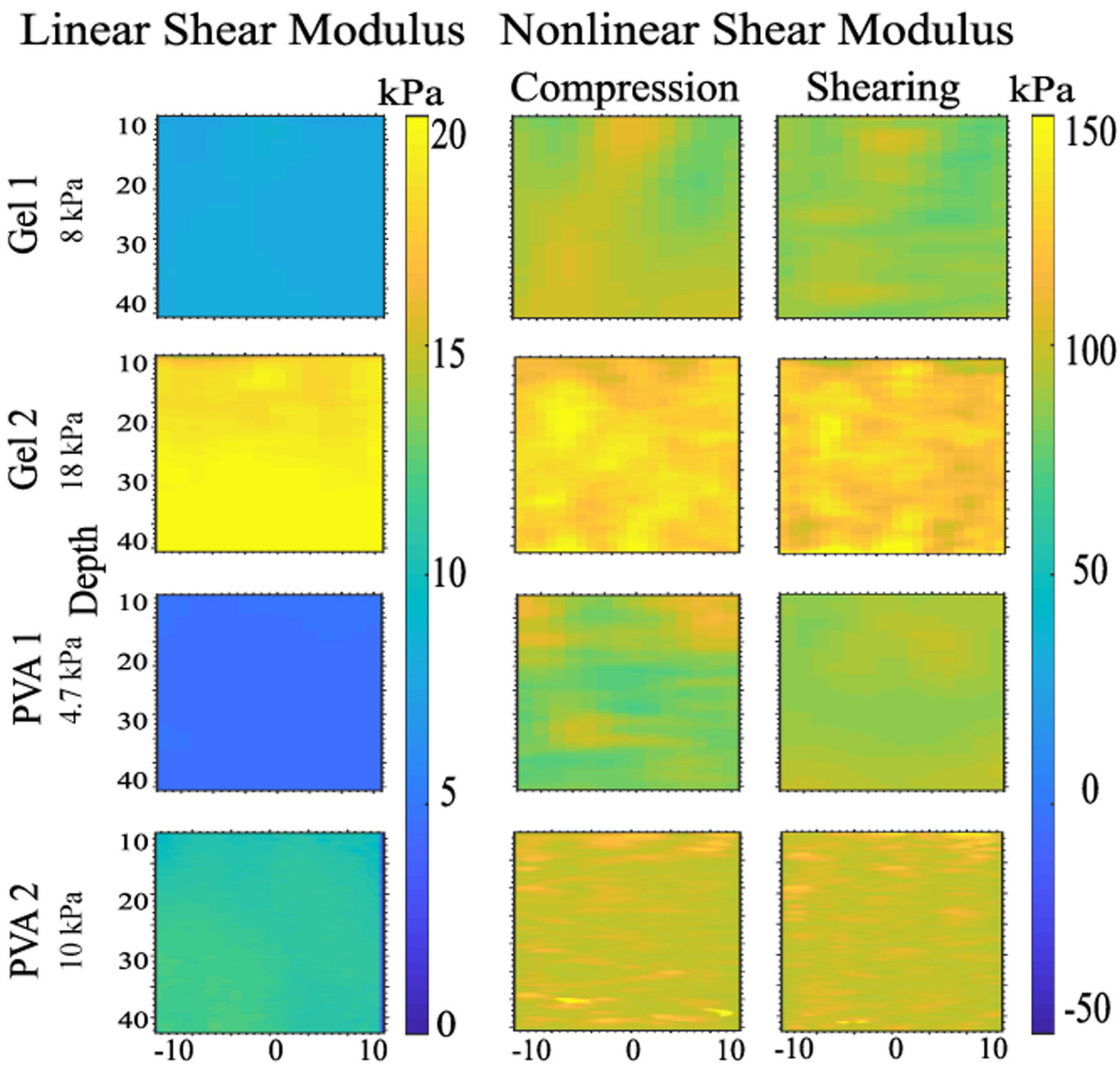

Fig. 8.

Results obtained for homogeneous gel and PVA phantoms. First column presents linear shear modulus maps, second and third column show estimated NLSM maps by pure compression and simple shearing. The true NLSM values were 91, 150.2 kPa for gel and 80.6, 112 kPa for PVA.

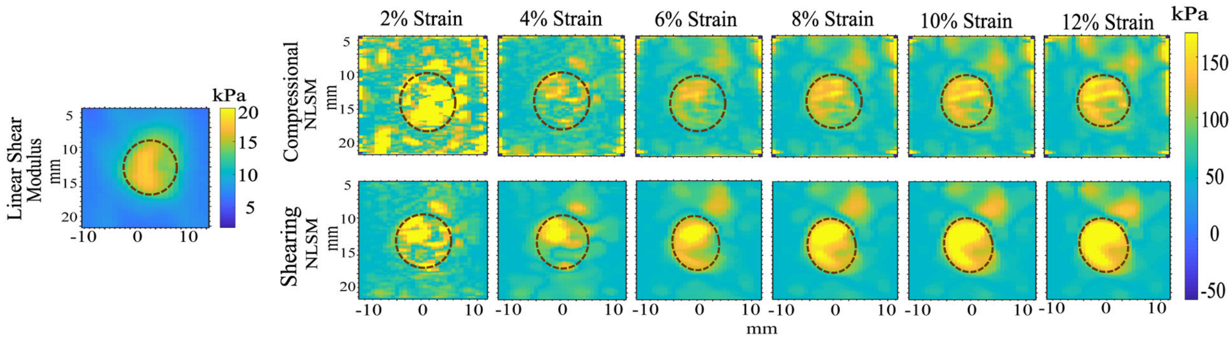

Fig. 9.

NLSM maps estimated by pure compression and simple shearing deformations for a 18 kPa inclusion in 8 kPa gelatin medium for different strain levels. The dotted circle shows the original inclusion position.

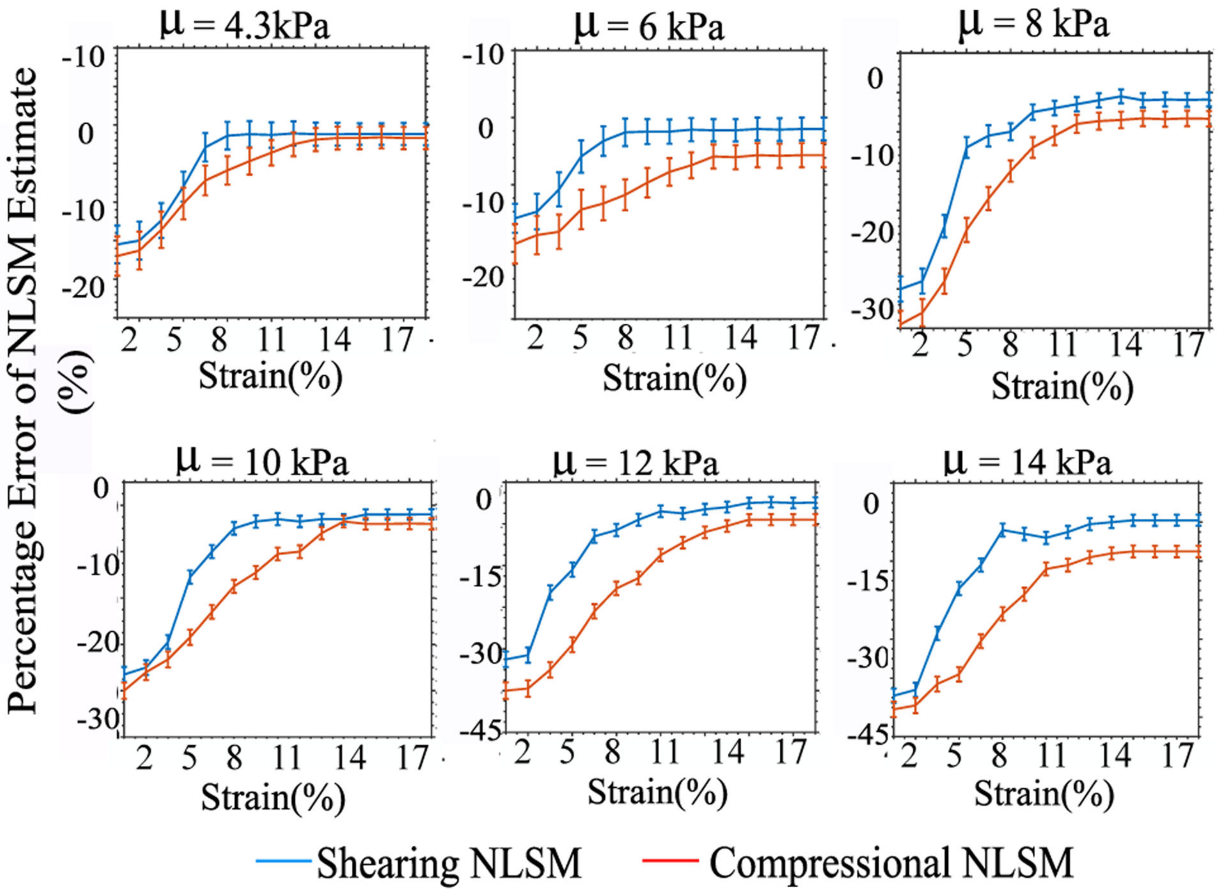

Fig. 10.

Plots showing percentage error or percentage bias of estimated NLSM at different strain levels for 6 different homogeneous phantoms. The % error is calculated by $\frac{|(A_T - A_M)|}{A_M}\%$ where A_T and A_M were the NLSM obtained by ultrasound and mechanical measurements, respectively. Shearing NLSM curve flattens and reaches asymptotic value faster than compression NLSM. Here the true values of NLSM were 35.2, 50, 91, 116.5, 136, 143.2 kPa respectively.

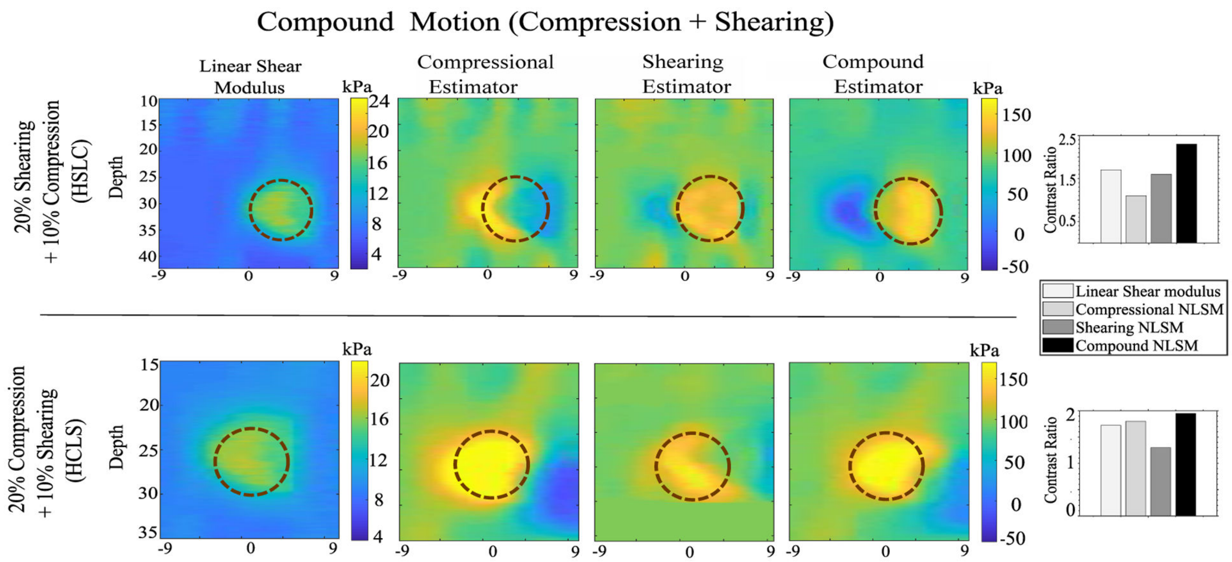

Fig. 11.

First column shows linear shear modulus images and the next three columns show NLSM images obtained by pure compressional, simple shearing and compound NLSM estimator. Two deformation types are shown, HSLC and HCLS deformation. The dotted circle shows the original inclusion position. The contrast ratio is obtained by $CR = \frac{\mu_I}{\mu_B}$, where μ_I and μ_B are the mean NLSM of inclusion and background respectively, obtained from a 3 × 3 mm window for both the inclusion and background.

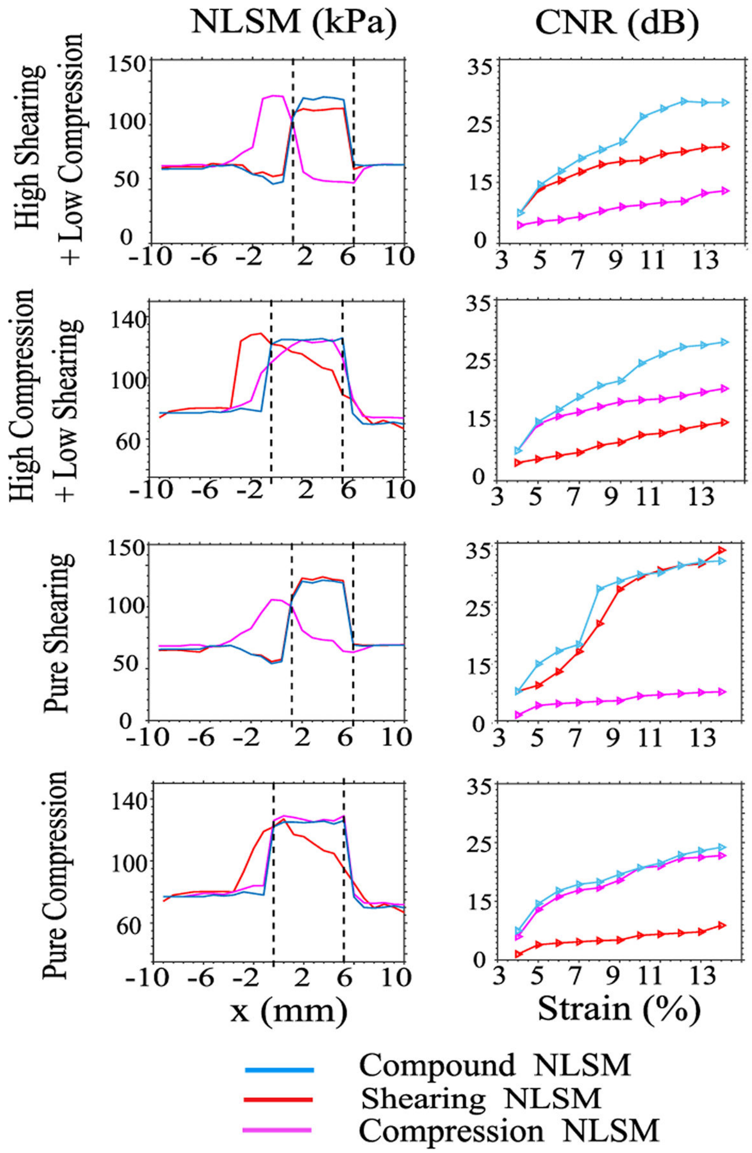

Fig. 12.

Estimated NLSM versus lateral position (left column) and CNR versus strain (right column) obtained in a gelatin inclusion phantom for each of the three NLSM expressions. Each row corresponds to the indicated deformation condition. NLSM plots lateral positions correspond to a cross-section through the 6.5 mm diameter stiff inclusion. Note that the compound estimator produces consistent values regardless of the deformation condition, and exhibits the highest CNR. Shear and compression estimators fail when the applied deformation is mismatched to the model.

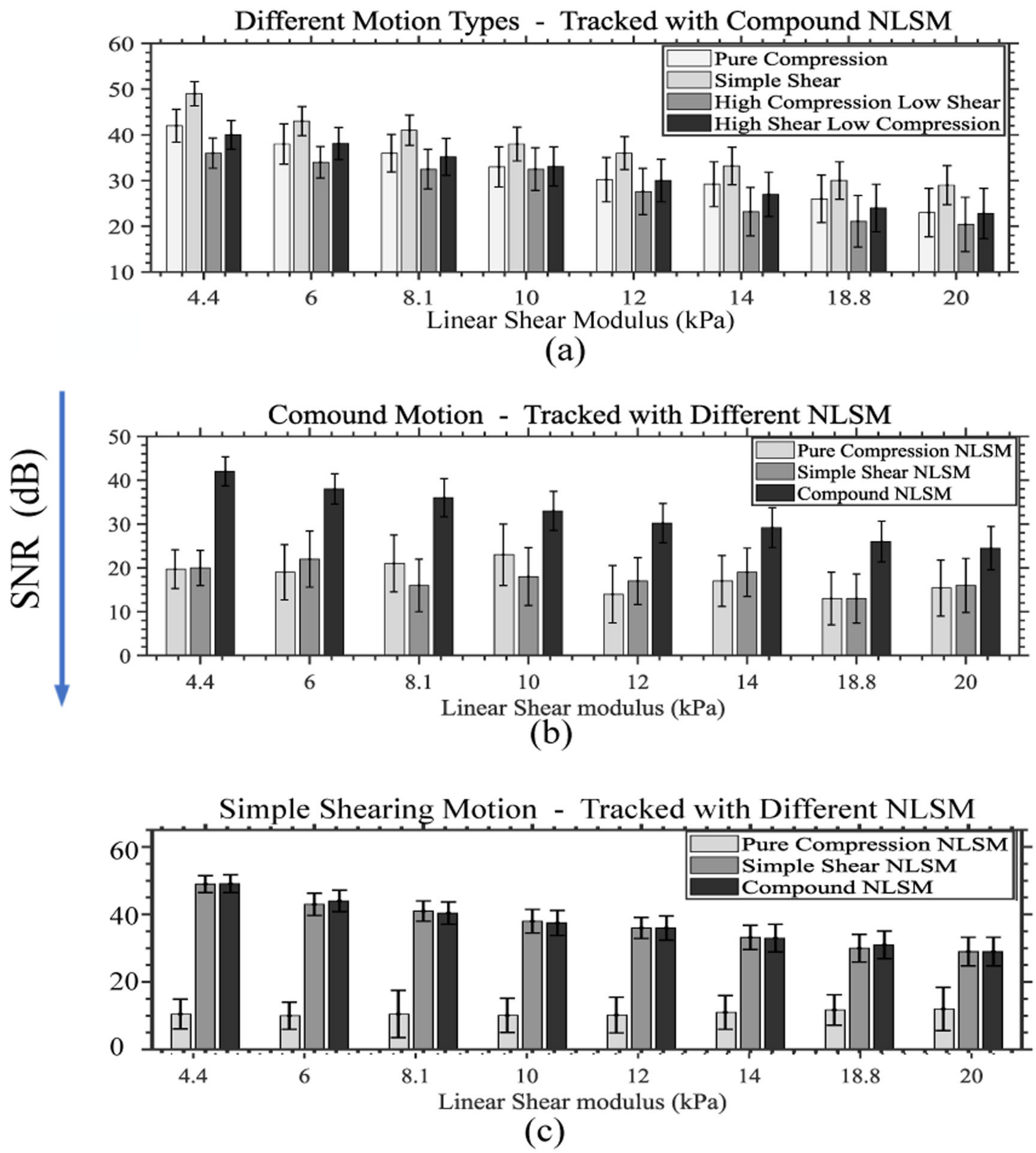

Fig. 13.

(a) represents bar plots of SNR for four deformation types to exhibit nonlinearity with reconstruction done by compound NLSM. (b) and (c) represents SNR for compound deformation and simple shearing, respectively, tracked by simple shear, pure compression and compound NLSM.